

## Article

# Enhancement of the Desorption Properties of $\text{LiAlH}_4$ by the Addition of $\text{LaCoO}_3$

Noratiqah Sazelee <sup>1</sup>, Nurul Amirah Ali <sup>1</sup>, Mohammad Ismail <sup>1,\*</sup>, Sami-Ullah Rather <sup>2</sup>, Hisham S. Bamufleh <sup>2</sup>, Hesham Alhumade <sup>2</sup>, Aqeel Ahmad Taimoor <sup>2</sup> and Usman Saeed <sup>2</sup>

<sup>1</sup> Energy Storage Research Group, Faculty of Ocean Engineering Technology and Informatics, Universiti Malaysia Terengganu, Kuala Nerus 21030, Terengganu, Malaysia; atiqahsazelee19@gmail.com (N.S.); nurullamirah@gmail.com (N.A.A.)

<sup>2</sup> Department of Chemical and Materials Engineering, King Abdulaziz University, P.O. Box 80204, Jeddah 21589, Saudi Arabia; rathersami@kau.edu.sa (S.-U.R.); hbamufleh@kau.edu.sa (H.S.B.); halhumade@kauedu.sa (H.A.); ataimoor@kau.edu.sa (A.A.T.); umsaeed@kau.edu.sa (U.S.)

\* Correspondence: mohammadismail@umt.edu.my; Tel.: +60-96-683-487

**Abstract:** The high hydrogen storage capacity (10.5 wt.%) and release of hydrogen at a moderate temperature make  $\text{LiAlH}_4$  an appealing material for hydrogen storage. However,  $\text{LiAlH}_4$  suffers from slow kinetics and irreversibility. Hence,  $\text{LaCoO}_3$  was selected as an additive to defeat the slow kinetics problems of  $\text{LiAlH}_4$ . For the irreversibility part, it still required high pressure to absorb hydrogen. Thus, this study focused on the reduction of the onset desorption temperature and the quickening of the desorption kinetics of  $\text{LiAlH}_4$ . Here, we report the different weight percentages of  $\text{LaCoO}_3$  mixed with  $\text{LiAlH}_4$  using the ball-milling method. Interestingly, the addition of 10 wt.% of  $\text{LaCoO}_3$  resulted in a decrease in the desorption temperature to 70 °C for the first stage and 156 °C for the second stage. In addition, at 90 °C,  $\text{LiAlH}_4 + 10$  wt.%  $\text{LaCoO}_3$  can desorb 3.37 wt.% of  $\text{H}_2$  in 80 min, which is 10 times faster than the unsubstituted samples. The activation energies values for this composite are greatly reduced to 71 kJ/mol for the first stages and 95 kJ/mol for the second stages compared to milled  $\text{LiAlH}_4$  (107 kJ/mol and 120 kJ/mol for the first two stages, respectively). The enhancement of hydrogen desorption kinetics of  $\text{LiAlH}_4$  is attributed to the in situ formation of AlCo and La or La-containing species in the presence of  $\text{LaCoO}_3$ , which resulted in a reduction of the onset desorption temperature and activation energies of  $\text{LiAlH}_4$ .

**Keywords:**  $\text{LiAlH}_4$ ;  $\text{LaCoO}_3$ ; solid-state hydrogen storage; metal oxide



**Citation:** Sazelee, N.; Ali, N.A.; Ismail, M.; Rather, S.-U.; Bamufleh, H.S.; Alhumade, H.; Taimoor, A.A.; Saeed, U. Enhancement of the Desorption Properties of  $\text{LiAlH}_4$  by the Addition of  $\text{LaCoO}_3$ . *Materials* **2023**, *16*, 4056. <https://doi.org/10.3390/ma16114056>

Academic Editors: Alessandro Dell'Era and Erwin Ciro Zuleta

Received: 16 April 2023

Revised: 24 May 2023

Accepted: 27 May 2023

Published: 29 May 2023



**Copyright:** © 2023 by the authors. Licensee MDPI, Basel, Switzerland. This article is an open access article distributed under the terms and conditions of the Creative Commons Attribution (CC BY) license (<https://creativecommons.org/licenses/by/4.0/>).

## 1. Introduction

Due to the world's population growth and civilizational developments, there has been an exponential increase in energy demand. The exploration of sustainable and renewable energy such as wind energy, hydropower, electrochemical energy and solar energy is believed to relieve the burden on the current energy demand [1–3]. Moreover, the amount of renewable energy consumed today is increasing which raises the standard for energy storage and transportation. However, the primary energy source is still fossil fuels despite the fact that they are unsustainable and have brought serious problems to the environment and human health [4,5]. Based on these facts, all countries have begun to implement a variety of strategies in order to avoid such problems. Future carbon emissions are predicted to be significantly reduced by hydrogen [6,7]. Over the last two decades, studies on hydrogen storage have received more attention in the literature [8,9]. In addition, hydrogen has the tremendous benefit of providing clean secondary energy with high energy content, no pollution and abundant resources [10,11]. There are three ways of storing hydrogen: (i) in a liquid form [12], (ii) in compressed gas [13] and (iii) in solid-state forms [14]. However, storing hydrogen in a solid-state form is attractive due to its safety reasons. The solid-state

form has two main types: (i) physisorption and (ii) chemisorption. In physisorption, the hydrogen binds in the molecular form to the surface of the host materials through weak interaction [15]. This physisorption process occurs for materials such as metal-organic frameworks [16] and carbon-based materials [17]. In 2023, a study by Mishra and colleagues [18] explored novel polycrystalline carbon nanotubes (PCNTs) in order to be used for large-scale hydrogen storage applications. They also revealed that PCNTs with moderate grain size are quite effective for these applications. Liang et al. [19] also reported an effective way to enhance hydrogen storage performance by using a porous carbon nanotube (CNT). However, the physisorption process has a low enthalpy of adsorption as revealed by previous studies [20,21]. Chemisorption is favorable because it can create a better storage capacity in ambient conditions [22]. Complex hydrides (such as  $\text{NaBH}_4$  and  $\text{LiAlH}_4$ ) and metal hydrides (such as  $\text{MgH}_2$ ) are typical materials for chemisorption. Other typical materials for chemisorption in chemical hydrogen storage are ammonia borane, methane, dimethyl ether, methanol, methanol and formic acid [23]. However, these chemical hydrides materials also suffer from some drawbacks, for example, ammonia borane ( $\text{NH}_3\text{BH}_3$ ) requires a long induction time and high temperature to release hydrogen [24] and ammonia ( $\text{NH}_3$ ) must be heated at high temperature (above  $650^\circ\text{C}$ ) to achieve complete conversion [25].

In this study, lithium aluminium hydride ( $\text{LiAlH}_4$ ), which are complex hydrides, have been used due to their low cost, moderate temperature to release hydrogen and high hydrogen storage capacity (10.5 wt.%) [26,27]. However, the use of  $\text{LiAlH}_4$  for hydrogen storage applications is still constrained by its sluggish kinetics and irreversibility [28,29]. Furthermore,  $\text{LiAlH}_4$  needs to be handled according to the safety data sheet and Standard Operating Procedure (SOP).  $\text{LiAlH}_4$  needs to be stored away from heat/flame and moisture/water sources and kept sealed under an inert atmosphere. Personal protective equipment including safety glasses, lab coat, gloves and covered shoes should be used. In order to overcome the disadvantages, a few techniques for enhancing its kinetics and thermodynamics have been investigated. For example, doping  $\text{LiAlH}_4$  with various kinds of catalysts or additives such as metal oxides [30–33], metal halides [34,35], metal hydrides [36], pure metals [37,38] and carbon material [39] have been performed via the ball-milling method. However, the improvement of  $\text{LiAlH}_4$  is adversely affected by the ball-milling technique as proposed by Resan and colleagues [40].

A study by Jiao and colleagues [41] revealed that excellent desorption properties of  $\text{LiAlH}_4$  were accomplished after being doped with 1 wt.% NiCo nanoalloy encapsulated in graphene layers (NiCo@G). The starting hydrogen release for the doped samples was unexpectedly lowered by  $109^\circ\text{C}$  compared to pure  $\text{LiAlH}_4$  ( $152^\circ\text{C}$ ). For the desorption kinetic performance, as-milled  $\text{LiAlH}_4$  releases 1.6 wt.% of  $\text{H}_2$  at  $150^\circ\text{C}$  within 10 min. Meanwhile, faster desorption kinetics can be observed after  $\text{LiAlH}_4$  is doped with 1 wt.% NiCo@G. The desorption kinetics for the doped samples carries on rapidly with 5.8 wt.% of  $\text{H}_2$  under the same conditions. As investigated by Li et al. [42], the addition of  $\text{CoFe}_2\text{O}_4$  nanopowder to  $\text{LiAlH}_4$  effectively lowered the decomposition kinetic barrier for  $\text{LiAlH}_4$ . Additionally, the activation energies of  $\text{LiAlH}_4$  doped with  $\text{CoFe}_2\text{O}_4$  for the first two stages were  $52.4\text{ kJ/mol}$  and  $86.5\text{ kJ/mol}$ , respectively. During the heating process of  $\text{LiAlH}_4$  doped with  $\text{CoFe}_2\text{O}_4$ , the  $\text{LiAlO}_2$ ,  $\text{LiFeO}_2$ ,  $\text{Al}_{0.52}\text{Co}_{0.48}$  and  $\text{Fe}_{0.98}\text{O}$  phases appeared in the X-ray diffraction (XRD) patterns, indicating that this reaction could alter the reaction thermodynamics by lowering the enthalpy of the desorption reaction. The improvement of  $\text{LiAlH}_4$  after the addition of  $\text{CoFe}_2\text{O}_4$  as a catalyst is also supported by Wei et al. [43]. It is exciting to note that they created  $\text{CoFe}_2\text{O}_4$  using a thermal decomposition method and discovered that the starts of hydrogen release as compared to pure  $\text{LiAlH}_4$  ( $176^\circ\text{C}$  and  $279^\circ\text{C}$  for the first two stages) were lowered by  $103.3^\circ\text{C}$  and  $97.9^\circ\text{C}$  for the first two stages, respectively.

Many studies have observed that rare earth metals such as Nb, Y and La exhibited excellent hydriding and dehydriding kinetics of  $\text{MgH}_2$  [44,45]. Additionally, adding 10 wt.%  $\text{LaFeO}_3$  lowered the activation energies and started the hydrogen release of  $\text{LiAlH}_4$  as indicated by our earlier research [46]. A further study discovered that the desorption

properties of  $\text{LiAlH}_4$  were greatly benefited by the freshly formed La or La-containing species, Fe and  $\text{LiFeO}_2$  that had been generated during the heating process. Based on the study by Zhou et al. [47], the reduction temperature in the endothermic peaks showed that the desorption properties of  $\text{LiAlH}_4$  were positively affected after the inclusion of  $\text{LaF}_3$ . On the other hand, Xueping et al. [48] looked into how the addition of  $\text{La}_2\text{O}_3$  affected the desorption properties of  $\text{LiAlH}_4\text{-NH}_4\text{Cl}$ . The result obtained shows that adding  $\text{La}_2\text{O}_3$  to  $\text{LiAlH}_4\text{-NH}_4\text{Cl}$  will increase the rate of hydrogen release while reducing the starting time.

In this context, with the aim of combining La and Co, Cobalt lanthanum oxide ( $\text{LaCoO}_3$ ) was introduced to prepare  $\text{LaCoO}_3\text{-LiAlH}_4$  via the ball-milling method to improve the hydrogen storage properties of  $\text{LiAlH}_4$ . Interestingly, various weight percentages of  $\text{LaCoO}_3$  were investigated to study the catalytic effects and the microstructure of hydrogen storage properties of  $\text{LiAlH}_4$ . To the best of the author's knowledge, no research on  $\text{LaCoO}_3$  and  $\text{LiAlH}_4$  performance has been published.

## 2. Materials and Methods

In this study,  $\text{LaCoO}_3$  was used as an additive and was synthesized using the solid-state method as discussed in our previous research [49]. A total of 0.121 g of citric acid ( $\geq 98\%$  pure; Sigma Aldrich, St. Louis, MO, USA), 0.081 g of lanthanum oxide ( $\geq 99.9\%$  pure; Aldrich Chemical Compound, Milwaukee, WI, USA) and 0.040 g of pure cobalt oxide (99.99% pure, Sigma Aldrich) were ground in an agate mortar and calcined at  $950\text{ }^\circ\text{C}$  in a furnace for 5 h. Different weight percentages of pure  $\text{LaCoO}_3$  (5, 10, 15 and 20) were milled in a planetary ball mill (NQM-0.4) with  $\text{LiAlH}_4$  (95% pure, Sigma Aldrich) for an hour (15 min milling time, 2 min resting time with 3 cycles) at a rotational speed of 400 rpm with a ball to powder ratio of 40:1. To prevent the reaction of samples with oxygen and moisture, all operations were conducted in an argon atmosphere glove box (MBRAUN UNILab, Germany) containing low concentrations of  $\text{O}_2$  ( $<0.1$  ppm) and  $\text{H}_2\text{O}$  ( $<0.1$  ppm) and high-purity Ar (99.99%).

The Gas Reaction Controller (GRC) evaluates quantitative analysis of the gas–solid reaction. It introduces a controlled amount of gas into the reaction chamber that holds a specimen. The pressure of the gas needs to be monitored while the temperature of the chamber is held constant or slowly changed. The instrument is connected to a computer and controlled by software (GrcLV), which performs fully automatic operations. Figure 1 below shows a schematic diagram of the working principles of the Sieverts apparatus. To determine the decomposition temperature of each sample, 150 mg of the materials were inserted into the sample holder and were heated at a rate of  $5\text{ }^\circ\text{C}/\text{min}$  from  $30$  to  $250\text{ }^\circ\text{C}$ . In the meantime, the desorption kinetics for all of the samples were heated for 80 min at  $90\text{ }^\circ\text{C}$ . This experiment was conducted by using Sievert-type apparatus (Advanced Materials Corporation, Pittsburgh, PA, USA).

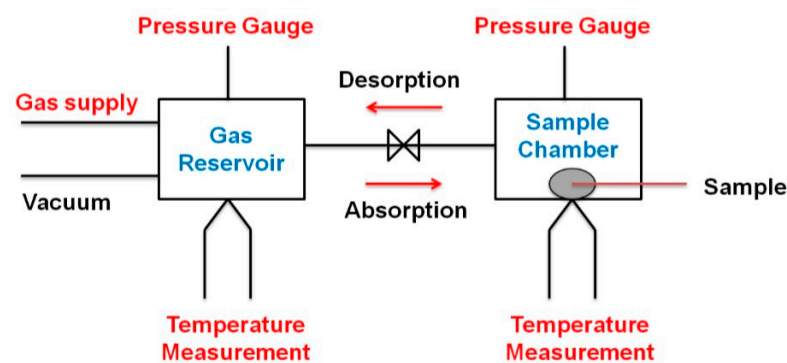


**Figure 1.** Schematic diagram showing the working principles of the Sieverts apparatus for determining hydrogen uptake/release.

Differential thermal analysis of the prepared samples was carried out using differential scanning calorimetry (Mettler Toledo, Columbus, OH, USA TGA/DSC 1) between  $30\text{--}300\text{ }^\circ\text{C}$

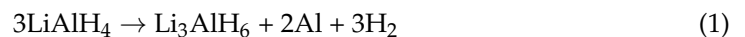
with a heating rate of 15, 20, 25 and 30 °C/min. Alumina crucibles were used as reference material. Samples weighing 6–8 mg were put into the crucible. The crucible was then sealed in a glass bottle to avoid the oxidation of the samples during the transfer from the glove box to the DSC apparatus. After the sample was placed inside the DSC, the gas inside the DSC was purged and constant argon flow (50 mL) was supplied. The designation of phase and composition of the samples were recorded by using XRD using Cu-K $\alpha$  radiation at room temperature at a scanning range of  $20^\circ < 2\theta < 80^\circ$ . To prevent the oxidation of the samples, a small amount of the sample was spread uniformly on the sample holder and covered with scotch tape and followed by sealing with plastic wrap as described in our previous studies [50,51]. Fourier transform infrared (FTIR) spectroscopy spectra were collected at room temperature at a resolution of  $4\text{ cm}^{-1}$  from  $800\text{ to }2000\text{ cm}^{-1}$ . For FTIR, the samples were placed in microcentrifuge tubes (1.5 mL) during transportation from the glove box. The samples were placed on the FTIR, and the measurement was analyzed for a few seconds. We had additionally taken some precautionary steps so that the exposure of the samples to the air is minimized. Meanwhile, the surface configuration of the samples was analyzed using scanning electron microscopy (SEM; JEOL, Akishima, Tokyo, Japan (JSM-6360LA)). Before each sample was analyzed, the samples were prepared on carbon tape and sprayed with a gold spray in a vacuum. Next, the samples were put in a sample container during the transfer process from the glove box to the SEM apparatus to prevent the samples from oxidizing. During the sample investigation, the samples were put inside the SEM under a vacuum state.

### 3. Results and Discussion

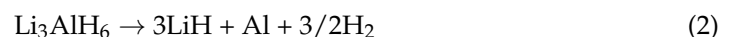
#### 3.1. Onset Desorption Temperature

The hydrogen release curves with temperature are shown in Figure 2 for pure LiAlH<sub>4</sub>, milled LiAlH<sub>4</sub> and LiAlH<sub>4</sub> with different weight percents of LaCoO<sub>3</sub>. A remarkable low-temperature shift was observed for hydrogen released from LiAlH<sub>4</sub> in the presence of LaCoO<sub>3</sub>. For pure LiAlH<sub>4</sub>, the first and second stages began at 151 °C and 182 °C, respectively with 7.39 wt.% of H<sub>2</sub> released. However, after LiAlH<sub>4</sub> was milled for an hour, the starting temperature release could be decreased from 151 °C to 147 °C and from 182 °C to 177 °C for the first and second stages, respectively, with 7.09 wt.% of the total H<sub>2</sub> released. It is validated that the milling of the samples used has a positive effect on the peak of the desorption temperature of LiAlH<sub>4</sub>. This statement was also proven by Liu et al. [36]. Theoretically, LiAlH<sub>4</sub> decomposes according to the following reactions [52,53]:

For the first stage,



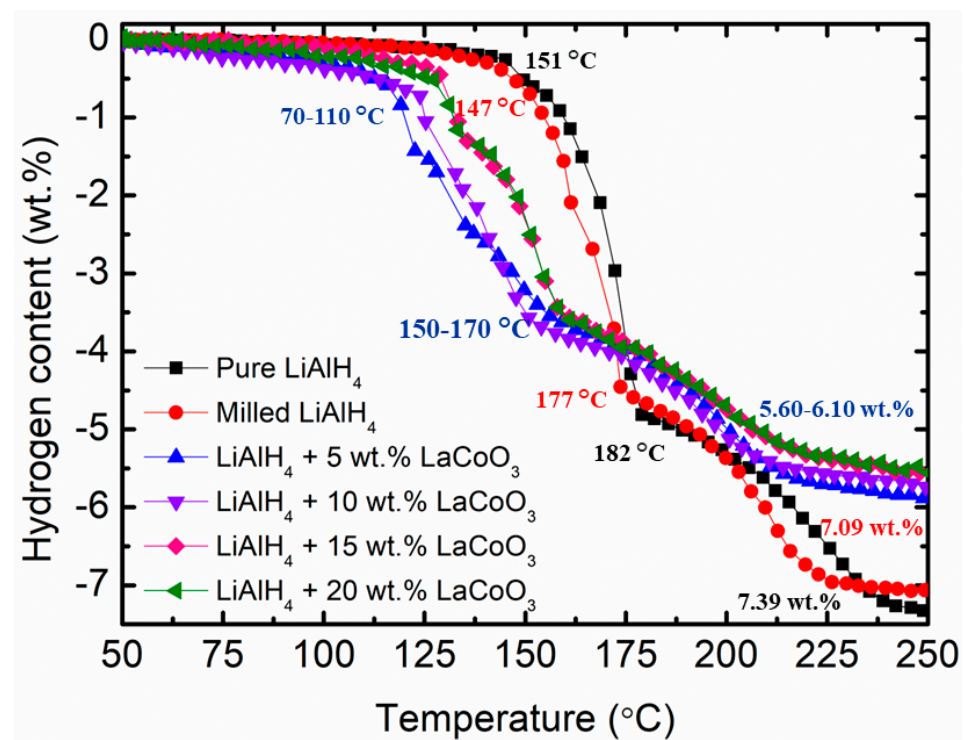
and for the second stage,



However, the temperature of onset desorption compared with milled LiAlH<sub>4</sub> was reduced from 147 °C to 98 °C and from 177 °C to 153 °C for the first and second stages, respectively, with 6.01 wt.% of H<sub>2</sub> released when 5 wt.% of LaCoO<sub>3</sub> was added. The desorption temperature drops to 70 °C and 105 °C for the first stage and 156 °C and 164 °C for the second stage, respectively, when 10 wt.% and 15 wt.% of LaCoO<sub>3</sub> are added. The total H<sub>2</sub> released for LiAlH<sub>4</sub> + 10 wt.% LaCoO<sub>3</sub> and LiAlH<sub>4</sub> + 15 wt.% LaCoO<sub>3</sub> were 5.86 wt.% and 5.72 wt.%, respectively. Increasing the amount of LaCoO<sub>3</sub> to 20 wt.% also lowered the onset desorption temperature by 45 °C and 13 °C compared with pure LiAlH<sub>4</sub> for the first and second stages, respectively. In spite of that, the amount of hydrogen released also decreased to 5.67 wt.%. This happens due to the zero hydrogen content in the LaCoO<sub>3</sub>; this outcome also has been testified by Xia et al. [54] and Ahmad et al. [55]. Table 1 summarizes the onset desorption temperature, hydrogen content and total hydrogen loss for pure LiAlH<sub>4</sub>, milled LiAlH<sub>4</sub> and different weight percentages of LaCoO<sub>3</sub> with LiAlH<sub>4</sub> composites.

**Table 1.** Onset desorption temperature, hydrogen content and hydrogen loss from each sample.

Samples	Onset Desorption Temperature (1st Stage) (°C)	Onset Desorption Temperature (2nd Stage) (°C)	Hydrogen Content (wt.%)	Hydrogen Loss (wt.%)
Pure LiAlH <sub>4</sub>	151	182	7.39	-
Milled LiAlH <sub>4</sub>	147	177	7.09	0.30
LiAlH <sub>4</sub> + 5 wt.% LaCoO <sub>3</sub>	98	153	6.01	1.38
LiAlH <sub>4</sub> + 10 wt.% LaCoO <sub>3</sub>	70	156	5.86	1.53
LiAlH <sub>4</sub> + 15 wt.% LaCoO <sub>3</sub>	105	164	5.72	1.67
LiAlH <sub>4</sub> + 20 wt.% LaCoO <sub>3</sub>	106	169	5.67	1.72

**Figure 2.** Onset desorption temperature of pure LiAlH<sub>4</sub>, milled LiAlH<sub>4</sub> and LiAlH<sub>4</sub> + x wt.% LaCoO<sub>3</sub> (x = 5, 10, 15 and 20).

### 3.2. Isothermal Desorption Kinetics

For practical applications, the desorption rate of hydrogen storage materials is a crucial characteristic. Hence, Figure 3 below shows the isothermal desorption kinetics for LiAlH<sub>4</sub> with different weight percents of LaCoO<sub>3</sub> composites compared to pure LiAlH<sub>4</sub> and milled LiAlH<sub>4</sub> at 90 °C within 80 min. Under the same conditions, the LiAlH<sub>4</sub> + 5 wt.% LaCoO<sub>3</sub> systems desorbed 3.37 wt.% of H<sub>2</sub>. Increasing the amount of LaCoO<sub>3</sub> to 10 wt.% also released 3.37 wt.% of H<sub>2</sub> under the same period. However, slightly faster desorption kinetics can be observed for LiAlH<sub>4</sub> + 5 wt.% LaCoO<sub>3</sub> systems within 30 min at 90 °C. Meanwhile, LiAlH<sub>4</sub> + 15 wt.% LaCoO<sub>3</sub> and LiAlH<sub>4</sub> + 20 wt.% LaCoO<sub>3</sub> composites release approximately 3.06 wt.% and 2.50 wt.% of H<sub>2</sub>, respectively. The individual LiAlH<sub>4</sub> releases less than 0.30 wt.% under the same conditions. This has proven that after the addition of LaCoO<sub>3</sub>, the isothermal desorption kinetics are 10 times faster than the unsubstituted LiAlH<sub>4</sub>. The next characterization was optimized to be 10 wt.% of LaCoO<sub>3</sub>. This is because the LiAlH<sub>4</sub> + 10 wt.% LaCoO<sub>3</sub> system decomposes at lower temperatures for the first stages compared to another amount of LaCoO<sub>3</sub>. Even though 5 wt.% also performed well for the isothermal desorption properties, the onset desorption temperature for 10 wt.% of LaCoO<sub>3</sub> compared to that of LiAlH<sub>4</sub> + 5 wt.% LaCoO<sub>3</sub> (98 °C) decreased by 28 °C for the first stages,

which indicates that the temperature for the  $\text{LiAlH}_4 + 5 \text{ wt.}\% \text{ LaCoO}_3$  is quite high for the desorption process to occur. Sulaiman and Ismail [56] also studied different weight percentages of  $\text{SrFe}_{12}\text{O}_{19}$  (10, 20 and 50) on the thermal desorption of  $\text{LiAlH}_4$ . A further study relating the catalytic effect of  $\text{SrFe}_{12}\text{O}_{19}$  on the hydrogen storage performance of  $\text{LiAlH}_4$  was performed using 10 wt.% of  $\text{SrFe}_{12}\text{O}_{19}$ . Next, the effects of 5, 10, 15 and 20 wt.% of  $\text{CoTiO}_3$  were investigated on the onset desorption temperature of  $\text{LiAlH}_4$  [57]. However, 10 wt.% of  $\text{CoTiO}_3$  was chosen as an optimal amount to explore the desorption properties of  $\text{LiAlH}_4$ . Thus, based on the discussion above, 10 wt.% of  $\text{LaCoO}_3$  was chosen for further characterization.

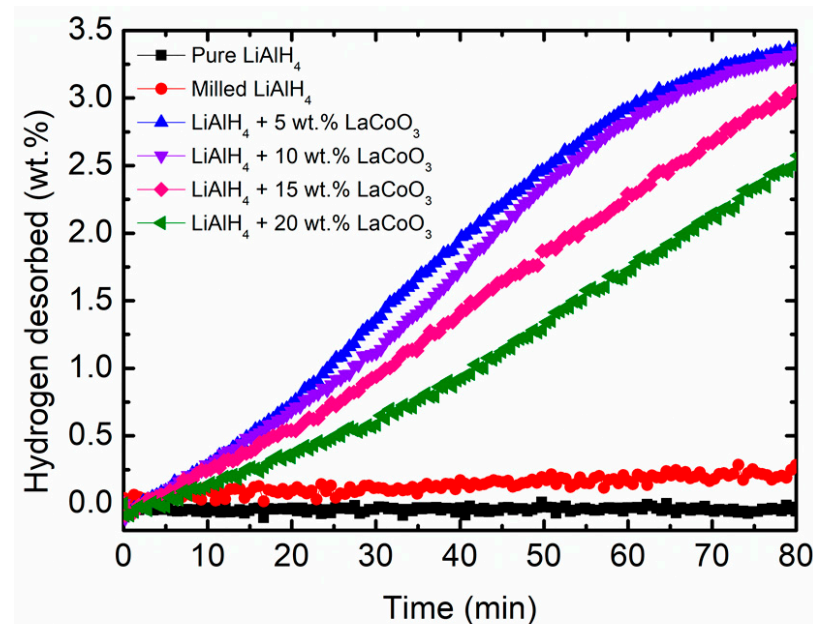


**Figure 3.** Isothermal desorption kinetics of pure  $\text{LiAlH}_4$ , milled  $\text{LiAlH}_4$  and  $\text{LiAlH}_4 + x \text{ wt.}\% \text{ LaCoO}_3$  ( $x = 5, 10, 15$  and  $20$ ).

### 3.3. Activation Energy

The DSC traces for milled  $\text{LiAlH}_4$  and  $\text{LiAlH}_4 + 10 \text{ wt.}\% \text{ LaCoO}_3$  are included in Figure 4a,b, respectively. The figure below indicates that as the heating rate increases, the temperature also increases. Figure 4c exhibits the comparison for milled  $\text{LiAlH}_4$  and  $\text{LiAlH}_4 + 10 \text{ wt.}\% \text{ LaCoO}_3$  at a heating rate of  $25 \text{ }^\circ\text{C}/\text{min}$ . For milled  $\text{LiAlH}_4$ , there are four peaks (two exothermic peaks and two endothermic peaks) [58,59]. At  $174 \text{ }^\circ\text{C}$ , the first exothermic peak can be regarded as being caused by  $\text{LiAlH}_4$  interacting with the surface hydroxyl impurities. These characteristics are due to the presence of surface hydroxyl impurities in the alanate powder, as already described in a previous study [60]. The second exothermic peak at  $220 \text{ }^\circ\text{C}$  was directly related to the decomposition of  $\text{LiAlH}_4$  to  $\text{Li}_3\text{AlH}_6$  and Al (as in Equation (1)) and the second endothermic peak at  $273 \text{ }^\circ\text{C}$  was believed to happen due to the decomposition of  $\text{Li}_3\text{AlH}_6$  to LiH and Al (as in Equation (2)). In contrast with the unsubstituted samples, the temperature of each peak dropped after the inclusion of 10 wt.%  $\text{LaCoO}_3$ . The first exothermic and endothermic peaks were  $134 \text{ }^\circ\text{C}$  and  $167 \text{ }^\circ\text{C}$ , respectively. Further heating led to additional exothermic and endothermic peaks at  $188 \text{ }^\circ\text{C}$  and  $242 \text{ }^\circ\text{C}$ , respectively. It has been shown that the addition of 10 wt.%  $\text{LaCoO}_3$  has shifted the peaks to a lower temperature for each reaction, proving that the desorption kinetics performance of  $\text{LiAlH}_4$  was improved. This could be associated with the fact that the introduction of 10 wt.%  $\text{LaCoO}_3$  leads to significant particle size refinement of  $\text{LiAlH}_4$ . The lower desorption peaks of the composite can effectively contribute to the kinetic improvement of  $\text{LiAlH}_4$  via the addition of 10 wt.%  $\text{LaCoO}_3$ . Furthermore,  $\text{LaCoO}_3$  is reported to have a hardness of 6.5 Mohs compared with the 4.0 Mohs of  $\text{LiAlH}_4$  [61]. The hardness of the  $\text{LaCoO}_3$  had thus broken the  $\text{LiAlH}_4$  particles. Therefore, smaller particle

size could enhance the kinetic enhancement and lower the activation energy of the  $\text{LiAlH}_4$ . The enhancement in the desorption kinetics performance is related to the energy barrier for hydrogen released from  $\text{LiAlH}_4$ .

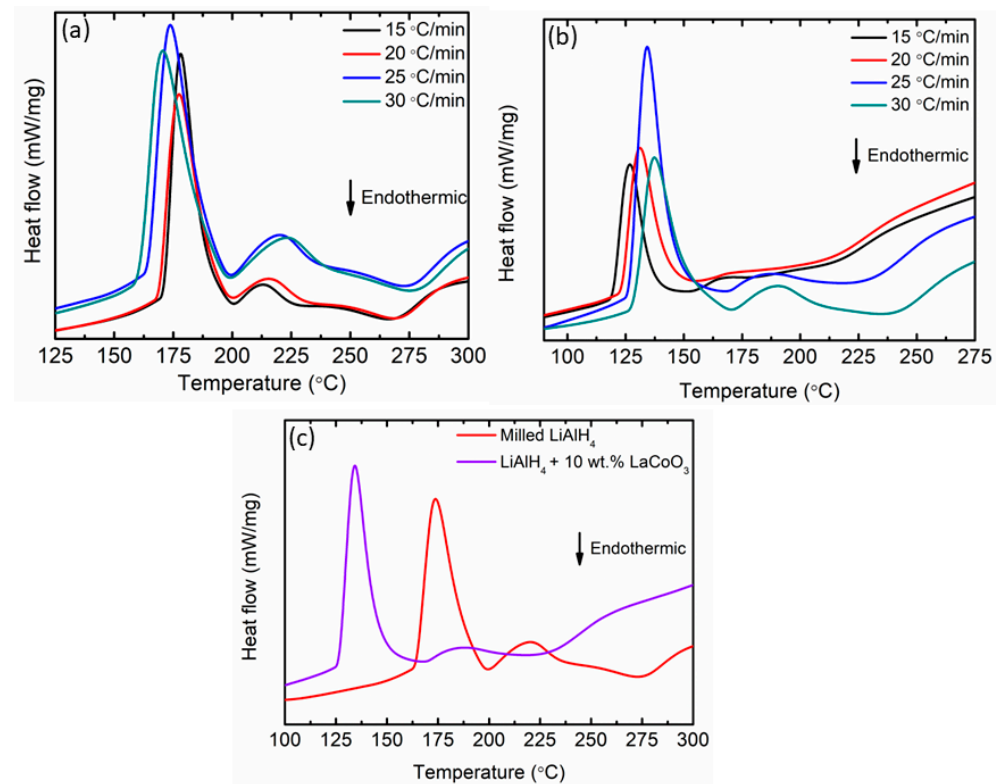


**Figure 4.** DSC traces of (a) milled  $\text{LiAlH}_4$ , (b)  $\text{LiAlH}_4 + 10 \text{ wt.}\% \text{ LaCoO}_3$  at various heating rates and (c) DSC traces at 25 °C/min of milled  $\text{LiAlH}_4$  and  $\text{LiAlH}_4 + 10 \text{ wt.}\% \text{ LaCoO}_3$ .

In order to obtain kinetic information of the hydrogen desorption from milled  $\text{LiAlH}_4$  and  $\text{LiAlH}_4 + 10 \text{ wt.}\% \text{ LaCoO}_3$ , the activation energies ( $E_A$ ) were examined using the Kissinger equation, as shown in Equation (3) below:

$$\ln [\beta/T_p^2] = -E_A/RT_p + A \quad (3)$$

where  $A$  = linear constant,  $R$  = gas constant,  $T_p$  = peak temperature in the DSC curve and  $\beta$  = heating rate. The activation value can be obtained by analyzing the slope of the Kissinger plot,  $\ln (\beta/T_p^2)$  vs.  $1000/T_p$ . The first stage of  $E_A$  was applied to the decomposition of  $\text{LiAlH}_4$  as shown in Figure 5a while the second stage of  $E_A$  was applied to the decomposition of  $\text{Li}_3\text{AlH}_6$  as illustrated in Figure 5b. From the figure, the  $E_A$  are 107 kJ/mol and 71 kJ/mol for milled  $\text{LiAlH}_4$  and  $\text{LiAlH}_4 + 10 \text{ wt.}\% \text{ LaCoO}_3$ , respectively. For the second stage, milled  $\text{LiAlH}_4$  has an  $E_A$  of 120 kJ/mol and this value decreased by 25 kJ/mol after the addition of 10 wt.%  $\text{LaCoO}_3$  (95 kJ/mol). This proves that adding  $\text{LaCoO}_3$  as an additive could lower the  $E_A$  of  $\text{LiAlH}_4$  for both stages. A previous study by Li et al. [62] exposed that the  $E_A$  of  $\text{LiAlH}_4$  are 78.2 kJ/mol and 90.8 kJ/mol, 38 kJ/mol and 42.2 kJ/mol lower than pure  $\text{LiAlH}_4$  for the first and second stages, respectively, after the addition of  $\text{K}_2\text{TiF}_6$ . Furthermore, Zhang et al. [63] revealed that the  $E_A$  was reduced by 18 kJ/mol for the first stages and 73.3 kJ/mol compared to milled  $\text{LiAlH}_4$  (90.6 kJ/mol and 144.7 kJ/mol) after adding  $\text{Li}_2\text{TiO}_3$ . Adding  $\text{SrFe}_{12}\text{O}_{19}$  also reduced the  $E_A$  from 103 kJ/mol to 76 kJ/mol for the first stage and from 111 kJ/mol to 96 kJ/mol for the second stage compared with milled  $\text{LiAlH}_4$  [56]. Based on this discussion, it can be concluded that adding  $\text{LaCoO}_3$  could lower the  $E_A$  of  $\text{LiAlH}_4$ . Owing to this reduction of the  $E_A$ , the desorption kinetics of  $\text{LiAlH}_4$  are enhanced.

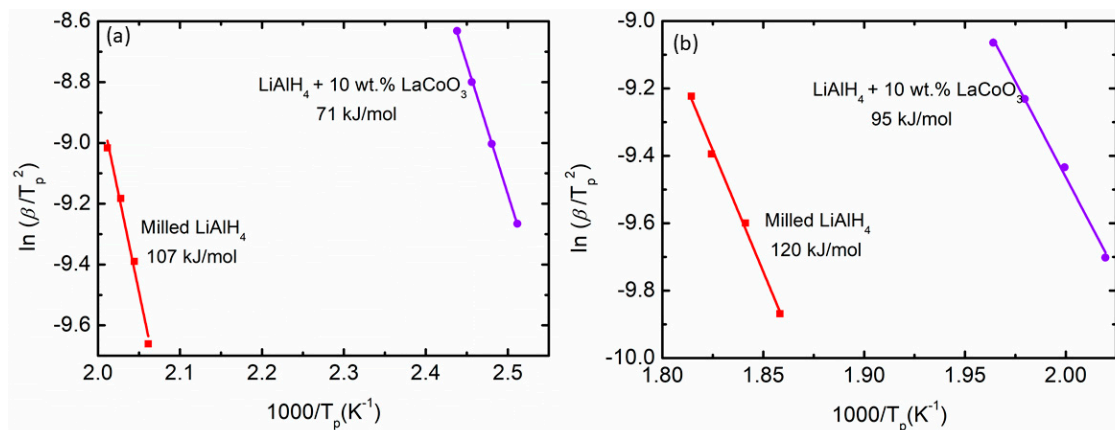


**Figure 5.** Activation energies of milled LiAlH<sub>4</sub> and LiAlH<sub>4</sub> + 10 wt.% LaCoO<sub>3</sub> for (a) first stages and (b) second stages.

### 3.4. Morphology and Microstructures

Figure 6 illustrates the SEM micrographs of pure LiAlH<sub>4</sub>, milled LiAlH<sub>4</sub> and LiAlH<sub>4</sub> + 10 wt.% LaCoO<sub>3</sub>. As shown in Figure 6a, the particles of pure LiAlH<sub>4</sub> are shaped like blocks and are coarse, as reported by a previous study [64]. After LiAlH<sub>4</sub> was milled for an hour, the particles became agglomerated and inhomogeneous, as shown in Figure 6b and proven by Ares and co-workers [65]. However, after the addition of LaCoO<sub>3</sub>, the particle size became small compared to pure LiAlH<sub>4</sub> and milled LiAlH<sub>4</sub> (Figure 6c). This result is consistent with earlier research showing that adding an additive or catalyst can reduce the particle size of LiAlH<sub>4</sub> [66]. In addition, after LiAlH<sub>4</sub> was doped with MnFe<sub>2</sub>O<sub>4</sub>, the samples decreased in particle size, resulting in more grain boundaries and increased surface area, which enhanced the desorption properties of LiAlH<sub>4</sub> [67]. Therefore, it can be concluded that after the addition of 10 wt.% LaCoO<sub>3</sub> through the ball-milling method, a smaller particle size can be observed, which may benefit the desorption behavior of the LiAlH<sub>4</sub>.

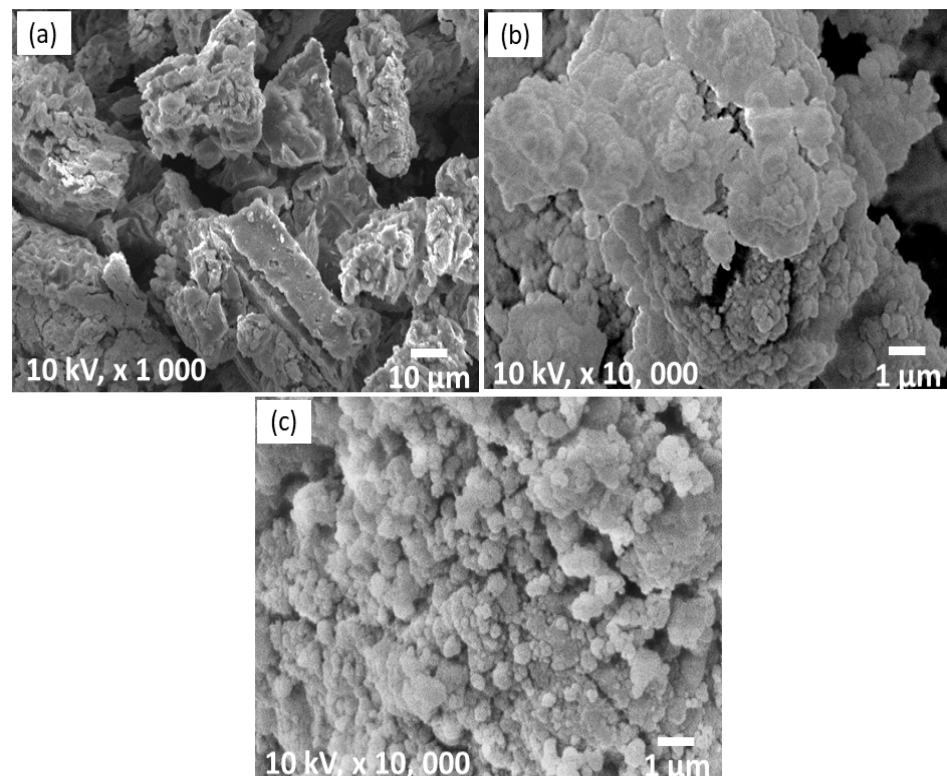


**Figure 6.** SEM images of (a) pure LiAlH<sub>4</sub>, (b) milled LiAlH<sub>4</sub> and (c) LiAlH<sub>4</sub> + 10 wt.% LaCoO<sub>3</sub>.

### 3.5. Particles Size Distribution

The data plotted in Figure 7 show the average particle size distribution (PSD) of composites with and without the addition of  $\text{LaCoO}_3$ . For pure  $\text{LiAlH}_4$  (as in Figure 7a), the particle size distribution calculated using ImageJ was  $39.62 \mu\text{m}$ . After an hour of the milling process of  $\text{LiAlH}_4$ , the samples improve the quality of the powders in terms of reduction in the particle size, as shown in Figure 7b. The particle size of milled  $\text{LiAlH}_4$  was reduced to  $0.66 \mu\text{m}$ . However, the particle size of  $\text{LiAlH}_4 + 10 \text{ wt.}\% \text{ LaCoO}_3$  is smaller if compared to the unsubstituted samples previously described in the SEM part. The average particle size of  $\text{LiAlH}_4 + 10 \text{ wt.}\% \text{ LaCoO}_3$  was  $0.27 \mu\text{m}$ , as shown in Figure 7c. In summary, the progressive phenomenon of reduction in particle size is reached, indicating that the inclusion of  $\text{LaCoO}_3$  using the ball-milling method improved the desorption performance of  $\text{LiAlH}_4$ .

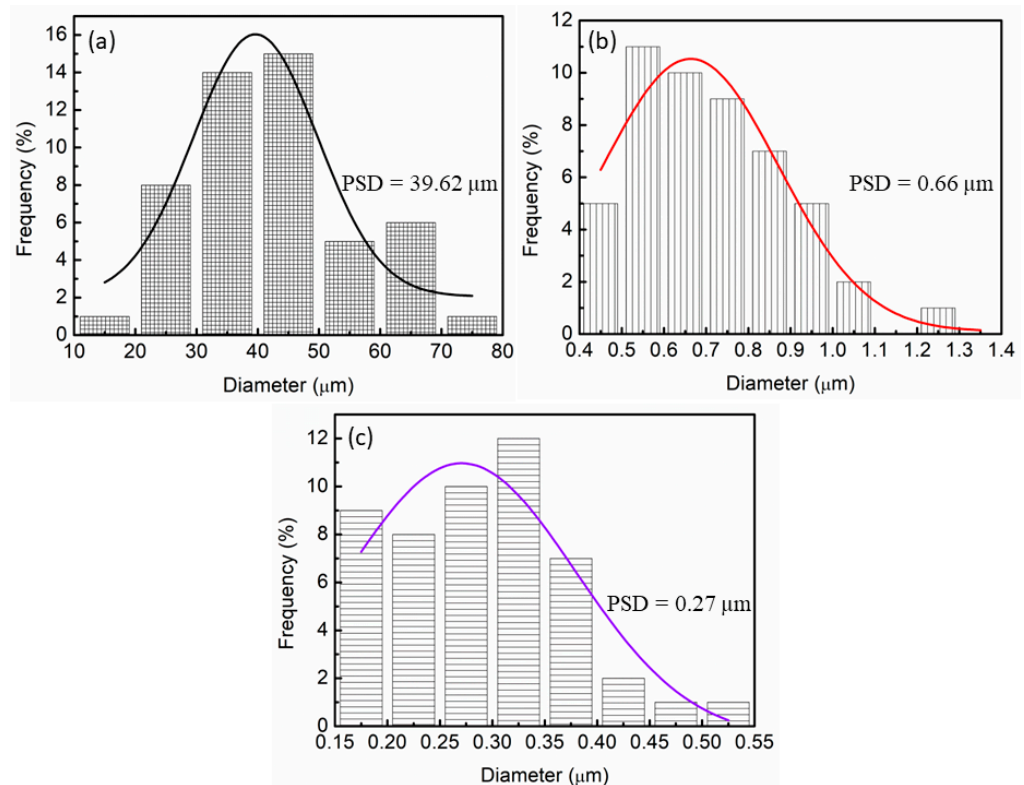


**Figure 7.** Particle size distributions of (a) pure  $\text{LiAlH}_4$ , (b) milled  $\text{LiAlH}_4$  and (c)  $\text{LiAlH}_4 + 10 \text{ wt.}\% \text{ LaCoO}_3$ .

### 3.6. Phase Structure

The XRD patterns of pure  $\text{LiAlH}_4$  and  $\text{LiAlH}_4$  after being milled for an hour are displayed in Figure 8a,b, respectively. At this stage, all the peaks correspond to  $\text{LiAlH}_4$ , which perfectly matches the standard pattern of  $\text{LiAlH}_4$  (JCPDS card no. 73-461). However, the intensity of the sample lowered compared to pure  $\text{LiAlH}_4$ . According to these patterns, the milling process will result in a reduction in the intensity of the peaks. A previous study by Rahmaninasab and colleagues [68] revealed that the milling time causes the intensity to be reduced. This is due to the increase in the lattice strain and internal energy during the milling process, as revealed by Dittrich et al. [69]. This also demonstrates that  $\text{LiAlH}_4$  is stable during the milling process, as stated in the previous studies [32,70,71]. The XRD pattern of  $\text{LiAlH}_4 + 10 \text{ wt.}\% \text{ LaCoO}_3$  is presented in Figure 8c. It was seen that the peaks related to  $\text{LiAlH}_4$  become broad and had a lower intensity when compared to unsubstituted  $\text{LiAlH}_4$ . No new peaks or peaks for  $\text{LaCoO}_3$  were detected during the milling process of  $\text{LaCoO}_3$ .

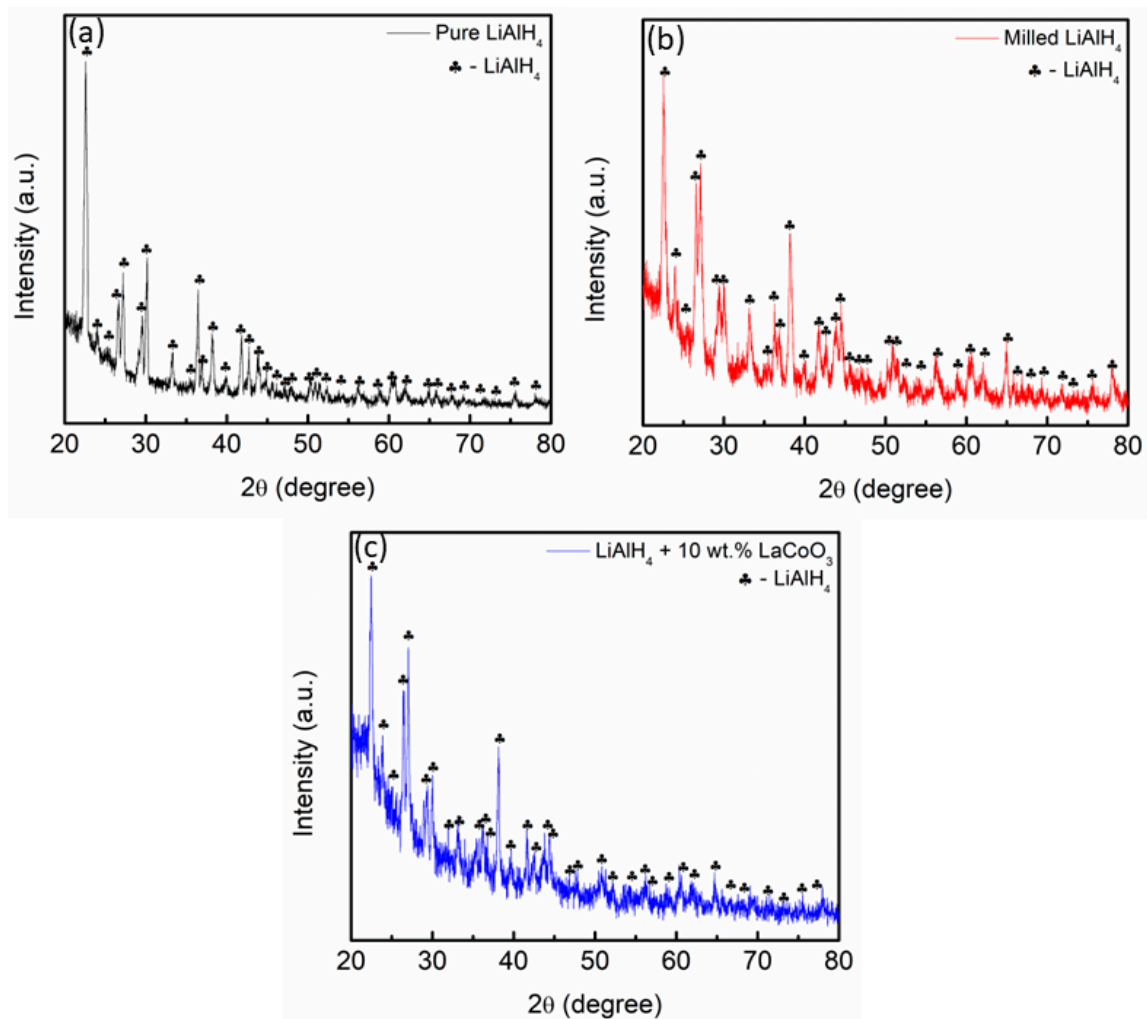


**Figure 8.** XRD pattern of (a) pure  $\text{LiAlH}_4$ , (b) milled  $\text{LiAlH}_4$  and (c)  $\text{LiAlH}_4 + 10 \text{ wt.}\% \text{ LaCoO}_3$ .

The FTIR spectra were carried out to confirm the presence of 10 wt.%  $\text{LaCoO}_3$ , as indicated in Figure 9. Two regions of active IR peaks that are the bending mode and the stretching mode were detected in the range of  $800\text{--}900 \text{ cm}^{-1}$  and  $1600\text{--}1800 \text{ cm}^{-1}$  [72], respectively, for pure  $\text{LiAlH}_4$ , milled  $\text{LiAlH}_4$  and  $\text{LiAlH}_4 + 10 \text{ wt.}\% \text{ LaCoO}_3$ . After the addition of 10 wt.%  $\text{LaCoO}_3$ , a new peak was detected at  $1383 \text{ cm}^{-1}$ , suggesting that  $\text{LiAlH}_4$  was decomposed to  $\text{Li}_3\text{AlH}_6$  and Al during the ball-milling process. A previous study led by Shen et al. [73] also revealed that the peaks that appear around  $1400 \text{ cm}^{-1}$  represent the stretching peak of  $\text{Li}_3\text{AlH}_6$ . Furthermore, after the addition of  $\text{NiFe}_2\text{O}_4$ , Wei et al. [43] discovered a weak stretching mode at about  $1404 \text{ cm}^{-1}$  which belongs to the Al–H stretching of  $[\text{AlH}_6]^{3-}$ .

To observe the change of phase structure of the  $\text{LiAlH}_4$  with  $\text{LaCoO}_3$  during the desorption process, an XRD scan has been conducted from  $20^\circ$  to  $80^\circ$ . As shown in Figure 10a below, after  $\text{LiAlH}_4 + 10 \text{ wt.}\% \text{ LaCoO}_3$  was heated, LiH and Al peaks were found, indicating that Equations (1) and (2) had occurred. A new peak for AlCo was identified, proving that the reaction of  $\text{LiAlH}_4$  and  $\text{LaCoO}_3$  may have occurred during the heating process. No peaks for La or La-containing species were detected as displayed in Figure 10a. However, after the amount of  $\text{LaCoO}_3$  was increased to 30 wt.% (as shown in Figure 10b), the same peaks for AlCo and LiH/Al were spotted.

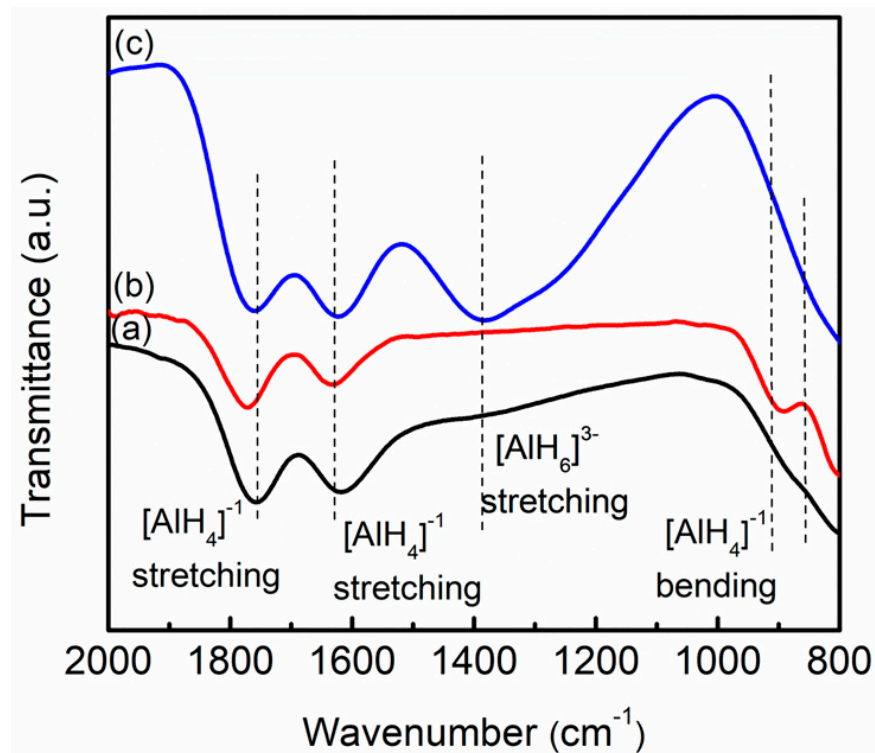


Figure 9. FTIR pattern of (a) pure LiAlH<sub>4</sub>, (b) milled LiAlH<sub>4</sub> and (c) LiAlH<sub>4</sub> + 10 wt.% LaCoO<sub>3</sub>.

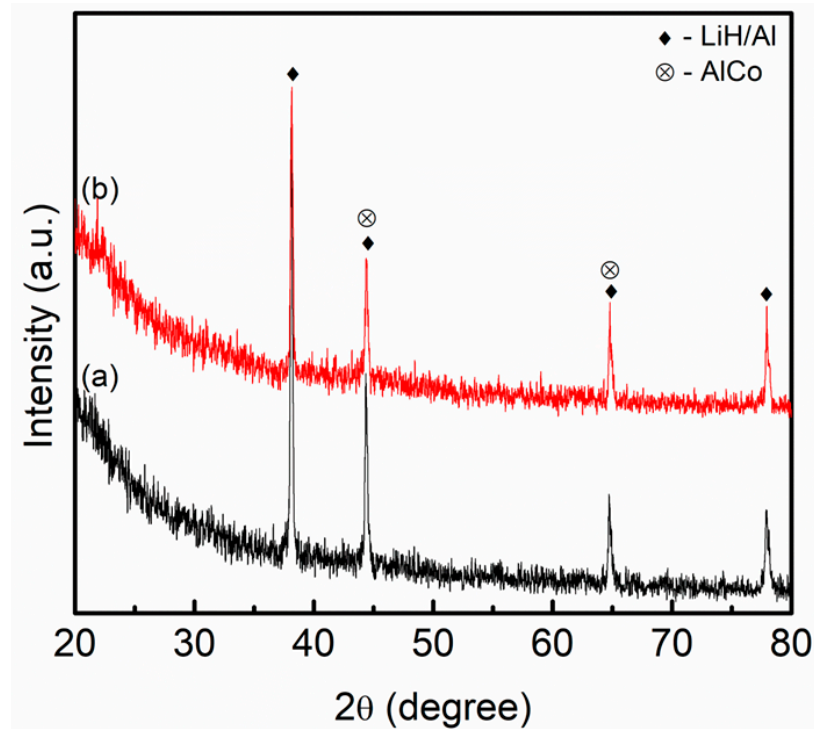


Figure 10. XRD pattern of (a) LiAlH<sub>4</sub> + 10 wt.% LaCoO<sub>3</sub> and (b) LiAlH<sub>4</sub> + 30 wt.% LaCoO<sub>3</sub> after desorption at 250 °C.

From the above discussions, the enhancement of LiAlH<sub>4</sub> may be ascribed to a few factors. The new active species of AlCo formed after the heating process acts as a real additive in enhancing the hydrogen storage performance of LiAlH<sub>4</sub>. Additionally, it has been evidenced that Co additives may benefit the desorption properties of light metal complex hydrides [74,75]. In addition, Lv and colleagues [76] managed to show that

the Co element significantly improves the hydrogen storage performance of the alloy. Other than that, Ali et al. [77] indicated that the formation of Al–Co alloys during the heating process of NaAlH<sub>4</sub> and CoTiO<sub>3</sub> is the cause of the enhanced desorption behavior of NaAlH<sub>4</sub>. Furthermore, the starting hydrogen released by NaAlH<sub>4</sub> compared to milled NaAlH<sub>4</sub> (200 °C) decreased by ~65 °C after the addition of CoTiO<sub>3</sub>. Moreover, hydrogen storage desorption of LiAlH<sub>4</sub> was improved by the presence of CoFe<sub>2</sub>O<sub>4</sub> nanoparticles [42]. The start of hydrogen release dropped to 65 °C at the first stage and the activation energy lowered by 42.4 kJ/mol in the presence of CoFe<sub>2</sub>O<sub>4</sub> nanoparticles. One of the reasons for the enhancement of LiAlH<sub>4</sub> is due to the formation of Al–Co phases during the heating process of LiAlH<sub>4</sub> and CoFe<sub>2</sub>O<sub>4</sub> composites. However, no peak for La or La-containing species (such as La–O, Co–La or Al–La) was detected due to the low amount of LaCoO<sub>3</sub> in the composite or La being amorphous. This result was consistent with our previous study [46]. Hence, it is possible to speculate in situ formation of AlCo and La or La-containing species during the heating process attributed to improving the desorption kinetics of LiAlH<sub>4</sub>.

#### 4. Conclusions

In this paper, thermal desorption of LiAlH<sub>4</sub> has been studied with and without the addition of different weight percentages of LaCoO<sub>3</sub> additive (5, 10, 15 and 20). It was found that the addition of 10 wt.% LaCoO<sub>3</sub> is an effective additive which substantially lowered the onset desorption temperature by 81 °C and 26 °C for LiAlH<sub>4</sub> compared with pure LiAlH<sub>4</sub> for the first two stages, respectively. Furthermore, the desorption kinetics are 10 times faster than the unsubstituted LiAlH<sub>4</sub> at 90 °C for 80 min. The LaCoO<sub>3</sub> additive considerably reduced the activation energies from 107 kJ/mol to 71 kJ/mol for the first stages and from 120 kJ/mol to 95 kJ/mol for the second stages. From our observation, the morphology of LiAlH<sub>4</sub> + 10 wt.% LaCoO<sub>3</sub> shows that the particle size becomes smaller and less agglomerate compared to the unsubstituted LiAlH<sub>4</sub>. The result of particle size distribution also proved that the addition of LaCoO<sub>3</sub> additive reduced the particle size to 0.27 μm, 39.35 μm lower than pure LiAlH<sub>4</sub> and 0.39 μm reduced from milled LiAlH<sub>4</sub>. Furthermore, the formation of new phases (AlCo and La or La-containing species) have a notable impact on enhancing the hydrogen storage behavior of LiAlH<sub>4</sub>, which can be determined by observing the reaction between LiAlH<sub>4</sub> and LaCoO<sub>3</sub> during the heating process.

**Author Contributions:** Writing—original draft, N.S. and M.I.; methodology, N.S.; writing—review and editing, N.A.A., S.-U.R., H.S.B., H.A., A.A.T. and U.S.; Visualization, N.A.A., S.-U.R., H.A., A.A.T. and U.S.; supervision, M.I. All authors have read and agreed to the published version of the manuscript.

**Funding:** This research work was funded by Institutional Fund Projects under grant no. (IFPIP: 407-135-1443). The authors gratefully acknowledge the technical and financial support provided by the Ministry of Education and King Abdulaziz University, DSR, Jeddah, Saudi Arabia.

**Institutional Review Board Statement:** Not applicable.

**Informed Consent Statement:** Not applicable.

**Data Availability Statement:** The data presented in this study are available on request from the corresponding author.

**Acknowledgments:** This research work was funded by Institutional Fund Projects under grant no. (IFPIP: 407-135-1443). The authors gratefully acknowledge technical and financial support provided by the Ministry of Education and King Abdulaziz University, DSR, Jeddah, Saudi Arabia.

**Conflicts of Interest:** The authors declare no conflict of interest.

#### References

1. Du, W.; Wang, X.; Zhan, J.; Sun, X.; Kang, L.; Jiang, F.; Zhang, X.; Shao, Q.; Dong, M.; Liu, H.; et al. Biological cell template synthesis of nitrogen-doped porous hollow carbon spheres/MnO<sub>2</sub> composites for high-performance asymmetric supercapacitors. *Electrochim. Acta* **2019**, *296*, 907–915. [[CrossRef](#)]
2. Wu, D.; Xie, X.; Zhang, J.; Ma, Y.; Hou, C.; Sun, X.; Yang, X.; Zhang, Y.; Kimura, H.; Du, W. Embedding NiS nanoflakes in electrospun carbon fibers containing NiS nanoparticles for hybrid supercapacitors. *Chem. Eng. J.* **2022**, *446*, 137262. [[CrossRef](#)]

3. Wu, D.; Xie, X.; Ma, Y.; Zhang, J.; Hou, C.; Sun, X.; Yang, X.; Zhang, Y.; Kimura, H.; Du, W. Morphology controlled hierarchical NiS/carbon hexahedrons derived from nitrilotriacetic acid-assembly strategy for high-performance hybrid supercapacitors. *Chem. Eng. J.* **2022**, *433*, 133673. [[CrossRef](#)]
4. Guo, X.; Liang, C.; Umar, M.; Mirza, N. The impact of fossil fuel divestments and energy transitions on mutual funds performance. *Technol. Forecast. Soc. Change* **2022**, *176*, 121429. [[CrossRef](#)]
5. Hansen, T.A. Stranded assets and reduced profits: Analyzing the economic underpinnings of the fossil fuel industry's resistance to climate stabilization. *Renew. Sust. Energ. Rev.* **2022**, *158*, 112144. [[CrossRef](#)]
6. Hienuki, S.; Noguchi, K.; Shibutani, T.; Fuse, M.; Noguchi, H.; Miyake, A. Risk identification for the introduction of advanced science and technology: A case study of a hydrogen energy system for smooth social implementation. *Int. J. Hydrogen Energy* **2020**, *45*, 15027–15040. [[CrossRef](#)]
7. Chapman, A.; Itaoka, K.; Farabi-Asl, H.; Fujii, Y.; Nakahara, M. Societal penetration of hydrogen into the future energy system: Impacts of policy, technology and carbon targets. *Int. J. Hydrogen Energy* **2020**, *45*, 3883–3898. [[CrossRef](#)]
8. Lebrouhi, B.E.; Djoupo, J.J.; Lamrani, B.; Benabdelaziz, K.; Kousksou, T. Global hydrogen development—A technological and geopolitical overview. *Int. J. Hydrogen Energy* **2022**, *47*, 7016–7048. [[CrossRef](#)]
9. Zhang, Y.; Zheng, J.; Lu, Z.; Song, M.; He, J.; Wu, F.; Zhang, L. Boosting the hydrogen storage performance of magnesium hydride with metal organic framework-derived Cobalt@Nickel oxide bimetallic catalyst. *Chin. J. Chem. Eng.* **2022**, *52*, 161–171. [[CrossRef](#)]
10. Zhang, J.; Hou, Q.; Guo, X.; Yang, X. Achieve high-efficiency hydrogen storage of MgH<sub>2</sub> catalyzed by nanosheets CoMoO<sub>4</sub> and rGO. *J. Alloys Compd.* **2022**, *911*, 165153. [[CrossRef](#)]
11. Nasser, M.; Megahed, T.F.; Ookawara, S.; Hassan, H. Techno-economic assessment of clean hydrogen production and storage using hybrid renewable energy system of PV/Wind under different climatic conditions. *Sustain. Energy Technol. Assess.* **2022**, *52*, 102195. [[CrossRef](#)]
12. Nasri, A.; Jaleh, B.; Shabanlou, E.; Nasrollahzadeh, M.; Ali Khonakdar, H.; Kruppke, B. Ionic liquid-based (nano)catalysts for hydrogen generation and storage. *J. Mol. Liq.* **2022**, *365*, 120142. [[CrossRef](#)]
13. Wang, H.; Zhao, Y.; Dong, X.; Yang, J.; Guo, H.; Gong, M. Thermodynamic analysis of low-temperature and high-pressure (cryo-compressed) hydrogen storage processes cooled by mixed-refrigerants. *Int. J. Hydrogen Energy* **2022**, *47*, 28932–28944. [[CrossRef](#)]
14. Sürer, M.G.; Arat, H.T. Advancements and current technologies on hydrogen fuel cell applications for marine vehicles. *Int. J. Hydrogen Energy* **2022**, *47*, 19865–19875. [[CrossRef](#)]
15. Sahoo, R.K.; Sahu, S. Transition from chemisorption to physisorption of H<sub>2</sub> on Ti functionalized [2,2,2]paracyclophane: A computational search for hydrogen storage. *J. Energy Storage* **2023**, *63*, 106951. [[CrossRef](#)]
16. Zhu, Z.W.; Zheng, Q.R. Investigation of cryo-adsorption hydrogen storage capacity of rapidly synthesized MOF-5 by mechanochemical method. *Int. J. Hydrogen Energy* **2023**, *48*, 5166–5174. [[CrossRef](#)]
17. Pandey, A.P.; Shaz, M.A.; Sekkar, V.; Tiwari, R.S. Synergistic effect of CNT bridge formation and spillover mechanism on enhanced hydrogen storage by iron doped carbon aerogel. *Int. J. Hydrogen Energy* **2022**, *in press, corrected proof*. [[CrossRef](#)]
18. Mishra, S.; Luhadiya, N.; Kundalwal, S.I. Atomistic insights into the H<sub>2</sub> adsorption and desorption behavior of novel Li-functionalized polycrystalline CNTs. *Carbon* **2023**, *207*, 23–35. [[CrossRef](#)]
19. Liang, H.; Du, X.; Li, J.; Sun, L.; Song, M.; Li, W. Manipulating active sites on carbon nanotube materials for highly efficient hydrogen storage. *Appl. Surf. Sci.* **2023**, *619*, 156740. [[CrossRef](#)]
20. Desai, F.J.; Uddin, M.N.; Rahman, M.M.; Asmatulu, R. A critical review on improving hydrogen storage properties of metal hydride via nanostructuring and integrating carbonaceous materials. *Int. J. Hydrogen Energy* **2023**, *in press, corrected proof*. [[CrossRef](#)]
21. Meduri, S.; Nandanavanam, J. Materials for hydrogen storage at room temperature—An overview. *Mater. Today Proc.* **2023**, *72*, 1–8. [[CrossRef](#)]
22. Zhang, X.; Sun, Y.; Xia, G.; Yu, X. Light-weight solid-state hydrogen storage materials characterized by neutron scattering. *J. Alloys Compd.* **2022**, *899*, 163254. [[CrossRef](#)]
23. Pawelczyk, E.; Łukasik, N.; Wysocka, I.; Rogala, A.; Gebicki, J. Recent progress on hydrogen storage and production using chemical hydrogen carriers. *Energies* **2022**, *15*, 4964. [[CrossRef](#)]
24. Akbayrak, S.; Özkar, S. Ammonia borane as hydrogen storage materials. *Int. J. Hydrogen Energy* **2018**, *43*, 18592–18606. [[CrossRef](#)]
25. Andersson, J.; Grönkvist, S. Large-scale storage of hydrogen. *Int. J. Hydrogen Energy* **2019**, *44*, 11901–11919. [[CrossRef](#)]
26. Sazelee, N.; Ismail, M. Recent advances in catalyst-enhanced LiAlH<sub>4</sub> for solid-state hydrogen storage: A review. *Int. J. Hydrogen Energy* **2021**, *46*, 9123–9141. [[CrossRef](#)]
27. Feng, W.; Xue Ping, Z.; Xue Qin, M.; Yue Hui, D.; Xiao Yan, Z.; Zi Wei, X. Catalytic effects of FGO-Ni addition on the dehydrogenation properties of LiAlH<sub>4</sub>. *Int. J. Hydrogen Energy* **2022**, *47*, 26458–26467. [[CrossRef](#)]
28. Sazelee, N.; Ali, N.; Yahya, M.; Mustafa, N.; Halim Yap, F.; Mohamed, S.; Ghazali, M.; Suwarno, S.; Ismail, M. Recent advances on Mg–Li–Al systems for solid-state hydrogen storage: A Review. *Front. Energy Res.* **2022**, *10*, 875405. [[CrossRef](#)]
29. Graetz, J.; Wegrzyn, J.; Reilly, J.J. Regeneration of lithium aluminum hydride. *J. Am. Chem. Soc.* **2008**, *130*, 17790–17794. [[CrossRef](#)]
30. Li, Z.; Li, P.; Wan, Q.; Zhai, F.; Liu, Z.; Zhao, K.; Wang, L.; Lü, S.; Zou, L.; Qu, X. Dehydrogenation improvement of LiAlH<sub>4</sub> catalyzed by Fe<sub>2</sub>O<sub>3</sub> and Co<sub>2</sub>O<sub>3</sub> nanoparticles. *J. Phys. Chem. C* **2013**, *117*, 18343–18352. [[CrossRef](#)]

31. Ali, N.A.; Idris, N.H.; Sazelee, N.A.; Yahya, M.S.; Halim Yap, F.A.; Ismail, M. Catalytic effects of  $\text{MgFe}_2\text{O}_4$  addition on the dehydrogenation properties of  $\text{LiAlH}_4$ . *Int. J. Hydrogen Energy* **2019**, *44*, 28227–28234. [[CrossRef](#)]
32. Sazelee, N.A.; Yahya, M.S.; Ali, N.A.; Idris, N.H.; Ismail, M. Enhancement of dehydrogenation properties in  $\text{LiAlH}_4$  catalysed by  $\text{BaFe}_{12}\text{O}_{19}$ . *J. Alloys Compd.* **2020**, *835*, 155183. [[CrossRef](#)]
33. Ismail, M.; Ali, N.A.; Sazelee, N.A.; Suwarno, S. Catalytic effect of  $\text{Al}_2\text{TiO}_5$  on the dehydrogenation properties of  $\text{LiAlH}_4$ . *Int. J. Hydrogen Energy* **2022**, *47*, 31903–31910. [[CrossRef](#)]
34. Cao, Z.; Ma, X.; Wang, H.; Ouyang, L. Catalytic effect of  $\text{ScCl}_3$  on the dehydrogenation properties of  $\text{LiAlH}_4$ . *J. Alloys Compd.* **2018**, *762*, 73–79. [[CrossRef](#)]
35. Ismail, M.; Zhao, Y.; Yu, X.B.; Dou, S.X. Effects of  $\text{NbF}_5$  addition on the hydrogen storage properties of  $\text{LiAlH}_4$ . *Int. J. Hydrogen Energy* **2010**, *35*, 2361–2367. [[CrossRef](#)]
36. Liu, S.S.; Li, Z.B.; Jiao, C.L.; Si, X.L.; Yang, L.N.; Zhang, J.; Zhou, H.Y.; Huang, F.-L.; Gabelica, Z.; Schick, C. Improved reversible hydrogen storage of  $\text{LiAlH}_4$  by nano-sized  $\text{TiH}_2$ . *Int. J. Hydrogen Energy* **2013**, *38*, 2770–2777. [[CrossRef](#)]
37. Varin, R.A.; Zbroniec, L.; Czujko, T.; Wronski, Z.S. The effects of nanonickel additive on the decomposition of complex metal hydride  $\text{LiAlH}_4$  (lithium alanate). *Int. J. Hydrogen Energy* **2011**, *36*, 1167–1176. [[CrossRef](#)]
38. Xueping, Z.; Ping, L.; Fuqiang, A.; Guoqing, W.; Xuanhui, Q. Effects of Ti and Fe additives on hydrogen release from lithium alanate. *Rare Metal. Mat. Eng.* **2008**, *37*, 400–403. [[CrossRef](#)]
39. Tan, C.Y.; Tsai, W.T. Effects of Ni and Co-decorated MWCNTs addition on the dehydrogenation behavior and stability of  $\text{LiAlH}_4$ . *Int. J. Hydrogen Energy* **2015**, *40*, 14064–14071. [[CrossRef](#)]
40. Resan, M.; Hampton, M.D.; Lomness, J.K.; Slattery, D.K. Effect of  $\text{Ti}_x\text{Al}_y$  catalysts on hydrogen storage properties of  $\text{LiAlH}_4$  and  $\text{NaAlH}_4$ . *Int. J. Hydrogen Energy* **2005**, *30*, 1417–1421. [[CrossRef](#)]
41. Jiao, C.; Sun, L.; Xu, F.; Liu, S.S.; Zhang, J.; Jiang, X.; Yang, L. NiCo nanoalloy encapsulated in graphene layers for improving hydrogen storage properties of  $\text{LiAlH}_4$ . *Sci. Rep.* **2016**, *6*, 27429. [[CrossRef](#)] [[PubMed](#)]
42. Li, Z.; Zhai, F.; Wan, Q.; Liu, Z.; Shan, J.; Li, P.; Volinsky, A.A.; Qu, X. Enhanced hydrogen storage properties of  $\text{LiAlH}_4$  catalyzed by  $\text{CoFe}_2\text{O}_4$  nanoparticles. *RSC Adv.* **2014**, *4*, 18989–18997. [[CrossRef](#)]
43. Wei, S.; Liu, J.; Xia, Y.; Zhang, H.; Cheng, R.; Sun, L.; Xu, F.; Huang, P.; Rosei, F.; Pimerzin, A.A.; et al. Remarkable catalysis of spinel ferrite  $\text{XFe}_2\text{O}_4$  (X = Ni, Co, Mn, Cu, Zn) nanoparticles on the dehydrogenation properties of  $\text{LiAlH}_4$ : An experimental and theoretical study. *J. Mater. Sci. Technol.* **2022**, *111*, 189–203. [[CrossRef](#)]
44. Wu, C.; Wang, Y.; Liu, Y.; Ding, W.; Sun, C. Enhancement of hydrogen storage properties by in situ formed  $\text{LaH}_3$  and  $\text{Mg}_2\text{NiH}_4$  during milling  $\text{MgH}_2$  with porous  $\text{LaNiO}_3$ . *Catal. Today* **2018**, *318*, 113–118. [[CrossRef](#)]
45. Sazelee, N.A.; Idris, N.H.; Md Din, M.F.; Yahya, M.S.; Ali, N.A.; Ismail, M.  $\text{LaFeO}_3$  synthesised by solid-state method for enhanced sorption properties of  $\text{MgH}_2$ . *Results Phys.* **2020**, *16*, 102844. [[CrossRef](#)]
46. Sazelee, N.A.; Yahya, M.S.; Idris, N.H.; Md Din, M.F.; Ismail, M. Desorption properties of  $\text{LiAlH}_4$  doped with  $\text{LaFeO}_3$  catalyst. *Int. J. Hydrogen Energy* **2019**, *44*, 11953–11960. [[CrossRef](#)]
47. Zhou, S.; Zou, J.; Zeng, X.; Ding, W. Effects of  $\text{REF}_3$  (RE = Y, La, Ce) additives on dehydrogenation properties of  $\text{LiAlH}_4$ . *Int. J. Hydrogen Energy* **2014**, *39*, 11642–11650. [[CrossRef](#)]
48. Xueping, Z.; Qihua, M.; Zhen, F.; Feng, M.; Shenglin, L.; Xin, F.; Guo, X.; Jiaojiao, Z. Effect of  $\text{La}^{3+}$  on dehydrogenation capacity of the  $\text{LiAlH}_4 - \text{NH}_4\text{Cl}$  system. *Rare Metal. Mat. Eng.* **2014**, *43*, 2075–2078. [[CrossRef](#)]
49. Sazelee, N.; Md Din, M.F.; Ismail, M.; Rather, S.U.; Bamufleh, H.S.; Alhumade, H.; Taimoor, A.A.; Saeed, U. Effect of  $\text{LaCoO}_3$  synthesized via solid-state method on the hydrogen storage properties of  $\text{MgH}_2$ . *Materials* **2023**, *16*, 2449. [[CrossRef](#)]
50. Halim Yap, F.A.; Mustafa, N.S.; Ismail, M. A study on the effects of  $\text{K}_2\text{ZrF}_6$  as an additive on the microstructure and hydrogen storage properties of  $\text{MgH}_2$ . *RSC Adv.* **2015**, *5*, 9255–9260. [[CrossRef](#)]
51. Ismail, M. Effect of adding different percentages of  $\text{HfCl}_4$  on the hydrogen storage properties of  $\text{MgH}_2$ . *Int. J. Hydrogen Energy* **2021**, *46*, 8621–8628. [[CrossRef](#)]
52. Luo, Y.; Wang, Q.; Li, J.; Xu, F.; Sun, L.; Zou, Y.; Chu, H.; Li, B.; Zhang, K. Enhanced hydrogen storage/sensing of metal hydrides by nanomodification. *Mater. Today Nano* **2020**, *9*, 100071. [[CrossRef](#)]
53. He, Q.; Zhu, D.; Wu, X.; Dong, D.; Xu, M.; Tong, Z. Hydrogen desorption properties of  $\text{LiBH}_4/x\text{LiAlH}_4$  (x = 0.5, 1, 2) composites. *Molecules* **2019**, *24*, 1861. [[CrossRef](#)]
54. Xia, Y.; Zhang, H.; Sun, Y.; Sun, L.; Xu, F.; Sun, S.; Zhang, G.; Huang, P.; Du, Y.; Wang, J. Dehybridization effect in improved dehydrogenation of  $\text{LiAlH}_4$  by doping with two-dimensional  $\text{Ti}_3\text{C}_2$ . *Mater. Today Nano* **2019**, *8*, 100054. [[CrossRef](#)]
55. Ahmad, M.A.N.; Sazelee, N.A.; Ali, N.A.; Ismail, M. Enhancing the dehydrogenation properties of  $\text{LiAlH}_4$  using  $\text{K}_2\text{NiF}_6$  as additive. *Int. J. Hydrogen Energy* **2022**, *47*, 24843–24851. [[CrossRef](#)]
56. Sulaiman, N.N.; Ismail, M. Catalytic effect of  $\text{SrFe}_{12}\text{O}_{19}$  on the hydrogen storage properties of  $\text{LiAlH}_4$ . *Int. J. Hydrogen Energy* **2017**, *42*, 19126–19134. [[CrossRef](#)]
57. Ali, N.A.; Ahmad, M.A.N.; Yahya, M.S.; Sazelee, N.; Ismail, M. Improved dehydrogenation properties of  $\text{LiAlH}_4$  by addition of nanosized  $\text{CoTiO}_3$ . *Nanomaterials* **2022**, *12*, 3921. [[CrossRef](#)]
58. Wei, S.; Xue, S.; Huang, C.; Che, B.; Zhang, H.; Sun, L.; Xu, F.; Xia, Y.; Cheng, R.; Zhang, C. Multielement synergetic effect of  $\text{NiFe}_2\text{O}_4$  and h-BN for improving the dehydrogenation properties of  $\text{LiAlH}_4$ . *Inorg. Chem. Front.* **2021**, *8*, 3111–3126. [[CrossRef](#)]
59. Li, Z.L.; Zhai, F.Q.; Qiu, H.C.; Wan, Q.; Li, P.; Qu, X.H. Dehydrogenation characteristics of ZrC-doped  $\text{LiAlH}_4$  with different mixing conditions. *Rare Met.* **2020**, *39*, 383–391. [[CrossRef](#)]

60. Ismail, M.; Sinin, A.; Sheng, C.; Nik, W. Desorption behaviours of lithium alanate with metal oxide nanopowder additives. *Int. J. Electrochem. Sci.* **2014**, *9*, 495.
61. Ismail, M.; Sazelee, N.A.; Ali, N.A.; Suwarno, S. Catalytic effect of SrTiO<sub>3</sub> on the dehydrogenation properties of LiAlH<sub>4</sub>. *J. Alloys Compd.* **2021**, *855*, 157475. [[CrossRef](#)]
62. Li, Z.; Liu, S.; Si, X.; Zhang, J.; Jiao, C.; Wang, S.; Liu, S.; Zou, Y.-J.; Sun, L.; Xu, F. Significantly improved dehydrogenation of LiAlH<sub>4</sub> destabilized by K<sub>2</sub>TiF<sub>6</sub>. *Int. J. Hydrogen Energy* **2012**, *37*, 3261–3267. [[CrossRef](#)]
63. Zhang, T.; Isobe, S.; Wang, Y.; Liu, C.; Hashimoto, N.; Takahashi, K. Enhanced hydrogen desorption properties of LiAlH<sub>4</sub> by doping lithium metatitanate. *Phys. Chem. Chem. Phys.* **2016**, *18*, 27623–27629. [[CrossRef](#)] [[PubMed](#)]
64. Varin, R.; Zbronic, L. Decomposition behavior of unmilled and ball milled lithium alanate (LiAlH<sub>4</sub>) including long-term storage and moisture effects. *J. Alloys Compd.* **2010**, *504*, 89–101. [[CrossRef](#)]
65. Ares, J.R.; Aguey Zinsou, K.F.; Porcu, M.; Sykes, J.M.; Dornheim, M.; Klassen, T.; Bormann, R. Thermal and mechanically activated decomposition of LiAlH<sub>4</sub>. *Mater. Res. Bull.* **2008**, *43*, 1263–1275. [[CrossRef](#)]
66. Li, L.; Qiu, F.; Wang, Y.; Xu, Y.; An, C.; Liu, G.; Jiao, L.; Yuan, H. Enhanced hydrogen storage properties of TiN–LiAlH<sub>4</sub> composite. *Int. J. Hydrogen Energy* **2013**, *38*, 3695–3701. [[CrossRef](#)]
67. Zhai, F.; Li, P.; Sun, A.; Wu, S.; Wan, Q.; Zhang, W.; Li, Y.; Cui, L.; Qu, X. Significantly improved dehydrogenation of LiAlH<sub>4</sub> destabilized by MnFe<sub>2</sub>O<sub>4</sub> nanoparticles. *J. Phys. Chem. C* **2012**, *116*, 11939–11945. [[CrossRef](#)]
68. Rahmaninasab, M.A.; Raygan, S.; Abdizadeh, H.; Pourabdoli, M.; Mirghaderi, S.H. Properties of activated MgH<sub>2</sub>+ mischmetal nanostructured composite produced by ball-milling. *Mater. Renew. Sustain. Energy* **2018**, *7*, 15. [[CrossRef](#)]
69. Dittrich, M.; Schumacher, G. Evolution of crystallite size, lattice parameter and internal strain in Al precipitates during high energy ball milling of partly amorphous Al<sub>87</sub>Ni<sub>8</sub>La<sub>5</sub> alloy. *Mater. Sci. Eng. A* **2014**, *604*, 27–33. [[CrossRef](#)]
70. Li, P.; Li, Z.; Zhai, F.; Wan, Q.; Li, X.; Qu, X.; Volinsky, A.A. NiFe<sub>2</sub>O<sub>4</sub> nanoparticles catalytic effects of improving LiAlH<sub>4</sub> dehydrogenation properties. *J. Phys. Chem. C* **2013**, *117*, 25917–25925. [[CrossRef](#)]
71. Ismail, M.; Zhao, Y.; Yu, X.B.; Nevirkovets, I.P.; Dou, S.X. Significantly improved dehydrogenation of LiAlH<sub>4</sub> catalysed with TiO<sub>2</sub> nanopowder. *Int. J. Hydrogen Energy* **2011**, *36*, 8327–8334. [[CrossRef](#)]
72. Prathana, C.; Aguey-Zinsou, K.F. Surfactant induced synthesis of LiAlH<sub>4</sub> and NaAlH<sub>4</sub> nanoparticles for hydrogen storage. *Appl. Sci.* **2022**, *12*, 4742. [[CrossRef](#)]
73. Shen, X.; Zhang, X.; Xiao, Q.; Liu, H. Catalytical enhancement on hydrogen production from LiAlH<sub>4</sub> by Fe–Fe<sub>2</sub>O<sub>3</sub> addition. *Int. J. Hydrogen Energy* **2022**, *47*, 16964–16977. [[CrossRef](#)]
74. Wang, Y.; Ren, Q.; Wang, Y.; Li, L.; Song, D.; Jiao, L.; Yuan, H. A facile two-step synthesis and dehydrogenation properties of NaAlH<sub>4</sub> catalyzed with Co–B. *Int. J. Hydrogen Energy* **2010**, *35*, 11004–11008. [[CrossRef](#)]
75. Hu, J.; Pohl, A.; Wang, S.; Rothe, J.; Fichtner, M. Additive effects of LiBH<sub>4</sub> and ZrCoH<sub>3</sub> on the hydrogen sorption of the Li–Mg–NH<sub>3</sub> hydrogen storage system. *J. Phys. Chem. C* **2012**, *116*, 20246–20253. [[CrossRef](#)]
76. Lv, L.; Lin, J.; Yang, G.; Ma, Z.; Xu, L.; He, X.; Han, X.; Liu, W. Hydrogen storage performance of LaNi<sub>3.95</sub>Al<sub>0.75</sub>Co<sub>0.3</sub> alloy with different preparation methods. *Prog. Nat. Sci. Mater.* **2022**, *32*, 206–214. [[CrossRef](#)]
77. Ali, N.A.; Ismail, M.; Nasef, M.M.; Jalil, A.A. Enhanced hydrogen storage properties of NaAlH<sub>4</sub> with the addition of CoTiO<sub>3</sub> synthesised via a solid-state method. *J. Alloys Compd.* **2023**, *934*, 167932. [[CrossRef](#)]

**Disclaimer/Publisher's Note:** The statements, opinions and data contained in all publications are solely those of the individual author(s) and contributor(s) and not of MDPI and/or the editor(s). MDPI and/or the editor(s) disclaim responsibility for any injury to people or property resulting from any ideas, methods, instructions or products referred to in the content.